Contents lists available at ScienceDirect

Materials Science and Engineering A
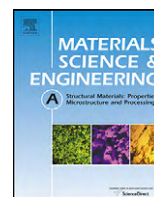
Study of the 1.25Cr–1Mo–0.25V steel microstructure after a carburization phenomenon

S. Simonetti [a,b,*], C. Lanz [c], G. Brizuela [a], A. Juan [a]

[a] *Departamento de Física, Universidad Nacional del Sur, Av. Alem 1253, 8000 Bahía Blanca, Argentina*
[b] *Departamentos de Ciencias Básicas e Ingeniería Mecánica, Universidad Tecnológica Nacional, 11 de Abril 461, 8000 Bahía Blanca, Argentina*
[c] *Departamento de Ingeniería, Universidad Nacional del Sur, Av. Alem 1253, 8000 Bahía Blanca, Argentina*

ARTICLE INFO

ABSTRACT

We studied the changes in the structure and carbide particle size in 1.25Cr–1Mo–0.25V steel under 600 °C and 168 MPa, after 4000 h service. We used microscopy and microanalysis techniques to analyze the carbide particles. We performed a complementary theoretical study on the chemical bonding and electronic structure of the carbide–Fe matrix interaction. The results contribute to the understanding of the changes in the alloy microstructure caused by the carburization phenomenon.

© 2010 Elsevier B.V. All rights reserved.

1. Introduction

If a material is exposed to gases containing carbon, e.g. in the form of CO, CO_2 or CH_4, it can pick up carbon. The degree of carburization is governed by the levels of carbon and oxygen in the gas, the temperature and the steel composition. The carbon which is picked up by the steel will largely form carbides. Carbon pick-up causes embrittlement of stainless steel due to carbides formation, or even a network of carbides, in the grain boundaries as well as within the grains. The resistance to thermal cycling is reduced and, since carburization leads to an increase in volume, there is a danger of cracks developing in the material.

When ferritic steels are heated to temperatures above 950 °C, they suffer precipitation of carbides during the subsequent cooling, and this causes a decrease in both toughness and corrosion resistance. On the other hand, carbide precipitation in the austenitic and ferritic–austenitic steels occurs at the temperature range 550–800 °C.

The precipitates formed in the grain boundaries cause intergranular corrosion and, in extreme cases, even a decrease in toughness. However, after only short times at the critical temperature range, e.g. in the heat affected zone adjacent to welds, the risk of precipitation is very small for the low-carbon steels.

The ferrite–perlite steels, used in components of equipment, before service have a BCC Fe (or ferrite) structure with perlite (or bainite) forming bars of ferrite and Fe carbides (Fe_3C) [1]. After service, the microstructure presents transformations. The carbides change from bars to spheres affecting the mechanical properties of steels because the spheroid carbides weaken the structure and help the dislocation movement by reducing the intragranular anchorage [2]. Several authors have named the carbides as M_3C, M_6C and $M_{23}C_6$, where M is a mixture of metallic atoms. A different grade of damage related to spheroidization of carbides has been observed in 1Cr–0.5Mo ferritic steel tested in creep [3].

Joarder et al. have investigated the microstructure and mechanical properties of 1Cr–1Mo–0.25V steels after service. The spheroidization of the carbides has a notable effect in the resistance and ductility of these steels [4].

The formation of a protective surface oxide film provides initial protection against metal contamination, but the local rupture of surface oxide films allows rapid carbon diffusion into the alloys [5].

Fe-base alloys in CH_4/H_2 carburizing gas mixtures have been studied by Yin [6]. At 800 °C Fe-base alloys suffered external carburization and oxidation, and the external Cr-rich scale layers were continuous consisting of oxides and carbides. Carburization resistance primarily depends on the protection afforded by external continuous layers. At 1100 °C, extensive external carburization occurred, and external layers became discontinuous consisting of Cr/Fe-carbides or metallic CrFe phases.

Intergranular stress corrosion cracking (IGSCC) of two commercial alloys 600, conditions were investigated using constant

* Corresponding author at: Departamento de Física, Universidad Nacional del Sur, Av. Alem 1253, 8000 Bahía Blanca, Argentina. Fax: +54 0291 4595142.
   E-mail address: ssimonet@uns.edu.ar (S. Simonetti).

Table 1
Chemical composition of the 1.25Cr–1Mo–0.25V steel (wt%).

C	Cr	Mo	V	Mn	Si	Fe
0.14	1.2	0.95	0.24	–	–	Balance[a]
0.1–0.16	1.1–1.4	0.9–1.1	0.2–0.35	0.4–0.7	0.17–0.37	Balance[b]

[a] Spectromax analysis for the specimens used.
[b] According to MRTU 14-4-21-67 Norm.

extension rate tensile (CERT) tests [7]. Results showed IGSCC was the dominant failure mode in all samples. For the commercial alloy and controlled-purity alloys, the microstructure with grain-boundary carbides showed delayed crack initiation and shallower crack depths than did the intragranular carbide microstructure under all experimental conditions.

Dobrzansky and Hernas have found that the creep velocity in steady state is related to the type and fraction of the carbides present [8].

A model steel (Fe–W–C) has been used to study the effect of the precipitation of carbides at austenite grain surfaces, on the subsequent formation of allotriomorphic ferrite. The removal of potent austenite grain boundary nucleation sites by the precipitation of carbides retards the allotriomorphic ferrite transformation [9].

The effect of bulk carbon content (0.1, 0.006, and 0.005 wt%) and tempering temperature (550, 580, and 640 °C) on stability, chemical composition, and size of carbide particles in 540 ks tempered states of 2.6Cr–0.7Mo–0.3V steel have been studied. Characteristic Energy-Dispersive X-ray (EDX) spectra can be attributed to each of the identified carbides. The MC carbide is stable in all experimental states [10].

Cementite/Fe_3C carbide in commercial low-carbon steel after prolonged service in naphtha environment with traces of sulphur of 0.3 ppm and at a temperature of 200–220 °C has been examined. Cementite transformation and disintegration of the degraded carbide phase is connected with a release of carbon that diffuses into the steel in front of the sulphur diffusion zone. Beneath the steel surface a layer of low carbon content is formed, followed by a zone of higher carbon content [11].

In this paper we studied the carbides formed in 1.25Cr–1Mo–0.25V steel obtained of the tubes of the cracking furnace from a hydroelectric power plant after 4000 h of service at 600 °C and 168 MPa. We analyzed the changes in the microstructure using optical and scanning electron microscopy (SEM) and Energy Dispersive X-ray Spectroscopy (EDAX spectrometry). A complementary theoretical study was also performed. The changes in the electronic structure after carbide formation are addressed. Chemical bonding analysis is also considered in order to explain some fails observed experimentally in steels.

2. Experimental study

The material studied in this paper is the ferritic 1.25Cr–1Mo–0.25V steel corresponding to $15 \times 1\,MI\,\Phi$ denomination and MRTU 14-4-21-67 Russian Norm. The chemical composition is shown in Table 1. In order to analyze the changes in the structure, we compared two samples of 1.25Cr–1Mo–0.25V steel, the virgin material with the same one obtained of the tubes of the cracking furnace from a hydroelectric power plant after 4000 h of service at 600 °C and 168 MPa.

The specimens were prepared according to ASTME 3 Norm [12–16]. Standard metallographic preparation techniques, mechanical grinding and polishing followed by etching in 2% Nital were applied to the samples.

The specimens were analyzed by optical microscopy [17,18]. Metallographic examination was carried using an optical microscope (mark: LEICA), with analyzer of images QWIN. We observe
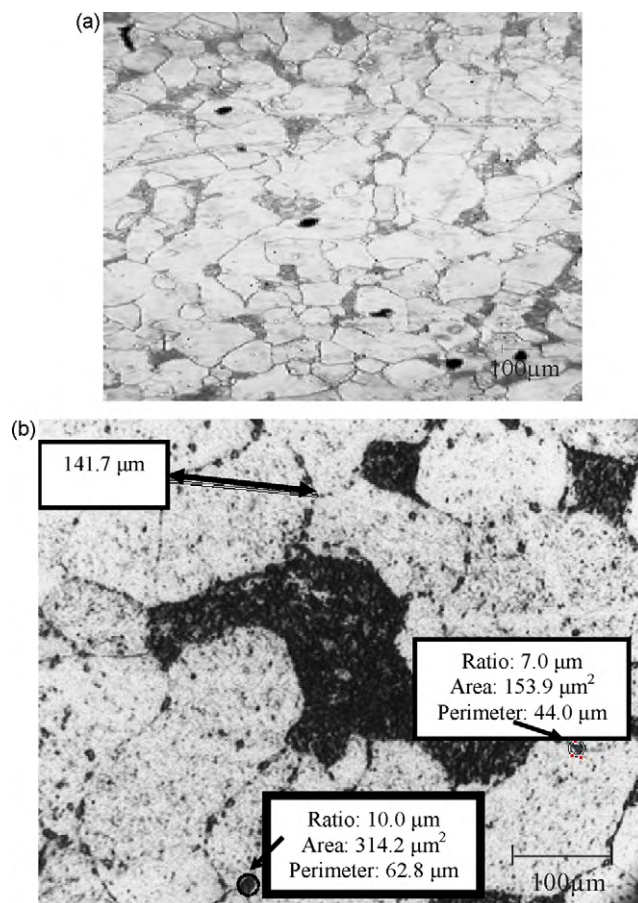

Fig. 1. Optical micrographs of (a) the original 1.25Cr–1Mo–0.25V alloy and (b) the 1.25Cr–1Mo–0.25V alloy tested at 600 °C and 168 MPa during 4000 h.

the virgin alloy microstructure forming equiaxial grains of ferrite with bainite colonies (Fig. 1(a)). In the service-exposed alloy, it is observed a fine precipitation of carbides in both, the bulk of ferrite grains and the grain boundaries (see Fig. 1(b)). The bainite forms a dispersed phase. The ferrite grain length is 140 μm and the carbides have average radius between 7 and 10 μm, perimeters of 44–65 μm and areas of 150–350 $μm^2$. The spherodization of carbides can also be observed. Intergranular carbide length of 0.28–0.57 μm, intergranular carbide thickness between 0.15 and 0.29 μm and coverage of intergranular carbide in grain boundary between 28 and 96% has been reported for Alloy 600 and Alloy 690 in caustic solution [19].

The specimens were also analyzed by scanning electron microscopy (SEM) [20–24] using a microscope JEOL JSM-35CF which operates at voltages between 1000 and 50,000 V and currents up to 10^{-7} A. The maximum magnification of the sample is 180,000×. From the SEM analysis, the virgin material presents ferrite grains (white zones) mixed with smaller portion of bainite colonies (black zones) (Fig. 2a), while the service-exposed material presents carbides that have coalesced and precipitated both, perimeter and inner grain boundaries (see Fig. 2(b)). Bainite colonies are detected and we can also see the presence of groups of carbides and fine dispersion of carbides in the matrix. We can also observe that the two microstructure finenesses are very different, both in the virgin state and in the aged state, which is not really surprising after such a long aging process.

Energy Dispersive X-ray Spectroscopy (EDAX) was used to determine the composition of the samples. The used EDAX microanalysis system (USA, 1994) allows the qualitative chemical analysis of microareas from Boron to Uranium. A system of digitalization of images (USA, 1994) containing the software of

Table 2
Chemical composition of the carbides in comparison with matrix composition for the 1.25Cr–1Mo–0.25V steel after service (4000 h at 600 °C and 168 MPa), obtained by EDAX spectromety.

	Matrix composition (wt%)	Carbide composition (wt%)
C	1.0	2.9
Mo	4.0	10.1
Cr	1.5	7.3
V	0.0	0.9
Fe	93.5	78.8

analysis and the statistics processing of images, complements the equipment. Table 2 shows the carbides and matrix chemical compositions of the 1.25Cr–1Mo–0.25V steel after service (4000 h at 600 °C and 168 MPa), obtained by EDAX spectrometry. We can observe that the C, Cr and Mo elements are in a higher proportion in the carbides than in the bulk matrix, while V is only present in the carbides. The carbides found in the 2.25Cr–1Mo steel are abundant in Fe with the orthorhombic structure of cementite (Fe_3C). Cr is soluble in the M_3C, while Mn and Mo are soluble in a smaller amount [1,25].

Transmission electron micrographs of specimens tempered for 100–200 h at a variety of temperatures for 2.25Cr–1Mo and 3Cr–1.5Mo steels show needle-shaped precipitates within the martensite laths [26]. Small and blocky spherical precipitates can be found on the lath boundaries. M_3C can be found in the early tempering stage with diskshape or bar-shape within laths and at the lath boundaries. M_2C could be easily identified from its needle shape within the laths.

By means of equilibrium calculations, Toh et al. predicted the formation of M_3C carbides at the surface of Fe–25Cr. The carbonization and dusting process was localized. These were shown by electron diffraction to be exclusively Fe_3C [27].

Mechanism and kinetics of carbide transformation during tempering at 700 °C have been studied in Fe–Mo–C steel (with up to 2.5% Mo) by transmission electron microscopy (TEM) and X-ray diffraction [28]. The sequence of carbide formation is $Fe_3C \rightarrow Mo_2C \rightarrow (Fe_2MoC, M_{23}C_6)$. Increasing the alloying element level increases the rate of carbide replacement reaction.

Ray et al. have described superheater and reheater 2.25Cr–1Mo steel boiler tubes from a thermal power plant after 17 years of service at nominally 537 °C and 40 MPa. A bainite–ferrite structure is observed, where the carbides are in the ferrite grains. At temperatures up to 600 °C, a resistance decrease is observed [29].

3. Computational study

A complementary theoretical study was performed to analyze the electronic structure and chemical bonding of the carbon–iron interaction. By cluster simulation using the YAeHMOP and ADF2000

programs [30–32], we performed calculations to compare the Fe structure before and after the Fe–C bond formation. According to that, we localized the C atom in the isolated Fe structure finding their minimum energy position. We can observe that the C atom locates near three Fe atoms at distances of 1.68, 1.75 and 1.77 Å, respectively. In an ab initio investigation of the diatomic iron carbide molecule, Tzeli and Mauridis report a C–Fe distance of 1.581 Å, which compares well the corresponding experimental data [31]. When investigating the effect of C on Fe-grain boundary cohesion by first principles, Wu et al. found a C–Fe distance on the (1 1 1) surface of 1.80 Å and 4% shorter than this value in the grain boundary environment [33]. Investigating the electronic and structural properties of cementite-type M_3X (M = Fe, Co, Ni; X = C or B) by first principles calculations, Shein et al. found M–X distances of 1.92–2.00 Å for carbides [34]. Additional calculations at DFT level included spin polarization; however the qualitative behavior of Fe–C interaction is the same as in the YAeHMOP calculations. Fig. 3 shows the contribution to the DOS including spin polarization.

Regarding the C location, it is known that carbon in the BCC Fe is located in the octahedral sites, namely in their c-sublattice, and the direction of polarization for Fe atom magnetic moments coincides with c-direction, which increases the space in the octahedral site because of positive volume magnetostriction. The C atom in the octahedral site causes tetragonal distortions, and two different Fe–C distances exist for two nearest Fe neighbors and four next-nearest Fe neighbors. The inset in Fig. 4 shows this octahedral distorted geometry for C.

The atomic orbital occupations of the C nearest neighbor metallic bonds are modified after the C location. The Fe 4s population decreases to about 16% when the C is present (see Table 3). The contribution of Fe 3d populations decreases an 11% while the Fe 4p population increases to about 6%. This indicates a majority participation of Fe 4s and Fe 3d orbitals in the C–Fe bonding. It is observed that the charge and the electronic structure of the more distant iron atoms are almost unaffected by the C atom. The electron densities of the atoms involved in the interactions are summarized in Table 3.

A strong bonding between C and Fe clusters can arise because of the nearness of the C valence levels to the s–d band of Fe
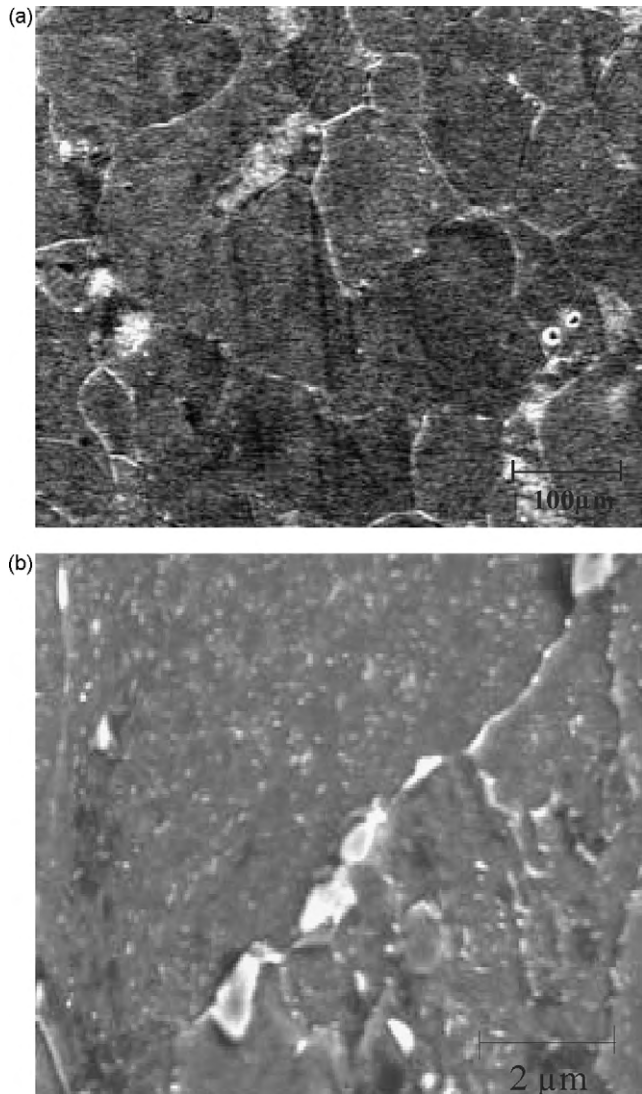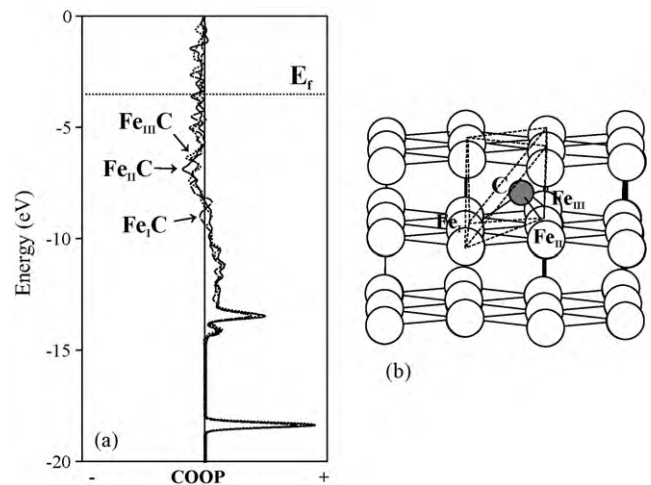
Fig. 4. (a) COOP curves for Fe–C interactions in the Fe cluster. (b) Schematic view of the carbon adsorption in the Fe cluster.

atomic levels and because of the availability of C 2p orbitals for better bonding interactions with Fe d orbitals. The resulting spatial anisotropy of bonding with the surrounding Fe atoms is the key factor determining the relative embrittling or cohesion enhancing behavior of a metalloid impurity. It was reported for Fe_3C that there are hybridized C 2p and Fe 3d states within the energy interval from -8 to -4 eV below E_f, which suggests covalent bonding between iron and carbon atoms [33]. For C on Ni(1 0 0) surface, Fourier et al. report that the carbon atom is strongly bound, essentially by a triple bond formed by the interaction of p_x, p_y and p_z orbitals of C with, primarily, the d orbitals of the four near Ni atoms [35].

Fig. 5 shows the Fe–Fe interaction, before and after carbide formation. The $Fe-Fe_{nn}$ (metallic bonds close to C) OP decreases to about 43% when the C atom is present. This bond weakening is mainly a consequence of the C–Fe interactions. The COOP curves for the Fe–C interactions can be seen in Fig. 4. As we can see, the C–Fe are bonding interactions. For the three Fe–C interactions (corresponding to distances of 1.68, 1.75 and 1.77 Å, respectively) we found Fe–C OP values of 0.774, 0.751 and 0.748, respectively.

The structure and stability of Fe_3C–cementite surfaces have been studied from first principles [36]. The authors show that greater stability is associated with localized Fe–C bonding at the surface, smoother surfaces created; e.g., by large C atom relaxation into the bulk and more uniform coordination at the surface. The relatively greater stability of Fe_3C surfaces is suggested to provide the driving force for cementite to form at the surfaces of BCC iron. Implications for the carburization erosion mechanism for steel, such as cracking and melting, are discussed.

Fig. 2. SEM micrographs of (a) the original 1.25Cr–1Mo–0.25V alloy and (b) the 1.25Cr–1Mo–0.25V alloy tested at 600 °C and 168 MPa during 4000 h.
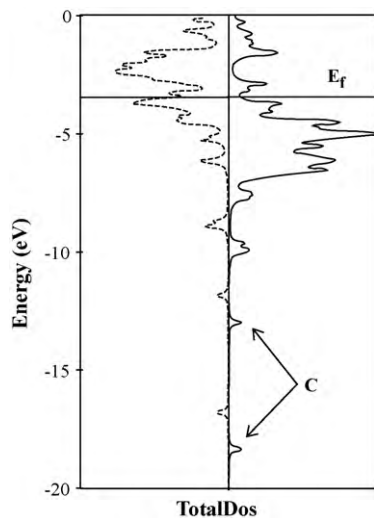

Fig. 3. Total DOS for the Fe cluster containing the C atom. The DOS for the spin-up state and spin-down state are shown in the left and right panel, respectively.

Table 3
Density orbital population for the C atom and their Fe nearest neighbors. Fe–C and Fe–Fe distances and the corresponding orbital overlap populations (OP).

Atom	s	p	d	Bond	Distance (Å)	OP	
C	1.482	4.068					
Fe	0.599	0.370	5.543[a]				
	0.714	0.347	6.243[b]	C–Fe$_I$	1.68	0.774	
				C–Fe$_{II}$	1.75	0.751	
				C–Fe$_{III}$	1.77	0.748	
				Fe–Fe$_{nn}$	2.48	0.158[a]	0.275[b]

Subscript nn: nearest neighbor.
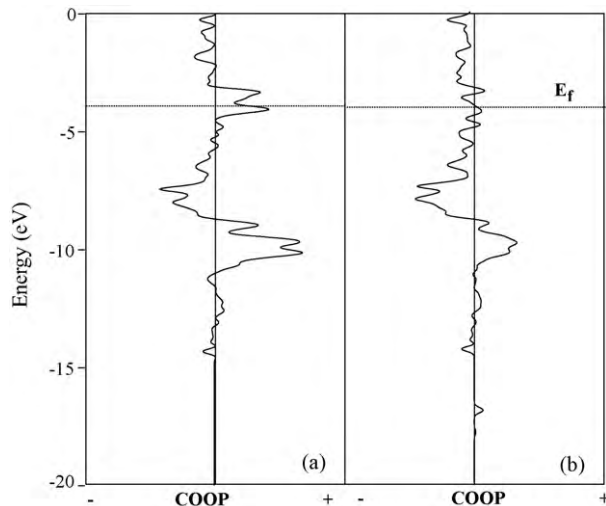[a] After C location.
[b] Before C location.

Fig. 5. COOP curves for Fe–Fe$_{nn}$ interaction (a) before and (b) after, C location.

4. Conclusions

We have analyzed the changes in the structure after the carburization phenomenon. We compared two samples of 1.25Cr–1Mo–0.25V steel, the virgin material with the same one obtained of the tubes of the cracking furnace from a hydroelectric power plant after 4000 h of service at 600 °C and 168 MPa. We observed a fine precipitate of carbides in both bulk and grain boundaries of ferrite in the service-exposed material. We determined the radius, perimeters and areas of the present carbides. The carbides spherodization was also detected. The SEM analysis showed the presence of carbides that have been coalesced and precipitated, both in the perimeter and inner grain boundaries in the service-exposed alloy. Groups of carbides and fine dispersion of carbides were also observed. We could observe that the C, Cr and Mo elements are present in a higher proportion in the carbides while V is only present in the carbide composition.

The theoretical calculations help us to interpret the changes in the electronic structure and chemical bonding. The atomic orbital occupations of the metallic bonds close to the C atom are affected after the C location. A majority participation of Fe 4s and Fe 3d orbitals in the C–Fe bonding is observed. The resulting spatial anisotropy of the Fe 3d–C 2p bonding is the key factor determining the relative embrittling or cohesion enhancing behavior of the C impurity. The Fe–Fe OP decreases to about 43% when the C atom is present as a consequence of the Fe–C interactions. This bond weakening could be related to the embrittlement phenomenon reported in Fe structures after carbide formation.

Acknowledgments

Appendix A.

A.1. The slab model and the computational method

α-Iron has a BCC structure with $a = 2.861$ Å and a nearest neighbor distance of 2.48 Å [37]. The (1 1 0) face is centered rectangular; to describe it we used a C(4 × 4) unit cell. The thickness of the α-Fe(1 1 0) slab should be such that it approximates the electronic structure of 3D bulk Fe in the innermost layer. In order to achieve the best compromise between computational time and accuracy of our model, we choose to use a seven layer slab. A part of the unit cell, $^{2}_{\infty}$[Fe]56, is shown as an inset in Fig. 4. The interlayer spacing in this Fe(1 1 0) model is 2.02 Å. The cell used was successfully used by Juan and Hoffmann [38]. We computed the adiabatic total energy of the system absorbing one carbon atom covering all the (0 0 1) planes. After determining the most stable position for the C atom, we studied the Fe–C interactions.

The calculations were performed using the ASED-MO (Atom Superposition and Electron Delocalization Molecular Orbital) method [39–42]. The modification of the extended Hückel Molecular Orbital method (EHMO) was implemented with the YAeHMOP program [30].

The adiabatic total energy values were computed as the difference between the electronic energy (E) of the system when the C atom is at finite distance within the bulk, and the same energy when that atom is far away from the solid surface.

The "carbon absorption energy" can be expressed as:

$$\Delta E_{total} = E(Fe_{56} + C) - E(Fe_{56}) - E(C) + E_{repulsion} \qquad (1)$$

The repulsive energy is computed taking into account all atom–atom interactions.

To understand the interactions between the atoms, we used the concept of COOP (crystal orbital overlap population) curves. The COOP curve is a plot of the overlap population weighted DOS (density of states) vs. energy. The integration of the COOP curve up to the Fermi level (E_f) gives the total overlap population of the bond specified and it is a measure of the bond strength.

Additional calculations were performed using gradient-corrected density functional theory (GC-DFT) [32]. The gradient correction, the Becke [43] approximation for the exchange energy functional and the B3LYP [44] approximation for the correlation functional were employed. In order to increase the computational efficiency, the innermost atomic shells of electrons are kept frozen for every atom except carbon, since the internal electrons do not contribute significantly to the bonding. We used a triple-zeta basis set (this means three Slater-type functions for each atomic valence orbital occupied) with polarization functions to express the atomic orbitals of Fe and C. The basis set of Fe consisted of 3p, 3d and 4s orbitals. In the cluster approach the bulk is modeled by a cluster of finite number of atoms. This approach was used successfully in recent years for FeAl alloys [45]. In metallic systems where a defect is screened by the electrons, a cluster in which the probe site is surrounded by atoms up by atoms up to the 2nd nearest neighbor shell has been found to be adequate [46]. The magnetic moment of the central Fe atom is 2.29 μB which compares very well with the magnetic moment of bulk iron of 2.20 μB.

References

[1] J.D. Parker, Proceeding of Ninth International Symposium, 1996, p. 122.
[2] J.H. Woodhead, A.G. Quarrell, J. Iron Steel Inst. 203 (1965) 605.
[3] L Toft, L. Marsden, Iron Steel Inst. 70 (1961) 276.
[4] A. Joarder, D.S. Sarma, N.S. Cheruvu, Metall. Trans. A 22 (1991) 1811.
[5] C. Chun, G. Bhargava, T. Ramanarayanan, J. Electrochem. Soc. (2007) 154.
[6] R. Yin, Mater. High Temp. 21 (2004).
[7] G. Was, K. Lian, Corrosion 54 (1998) 675.
[8] J. Dobrzanski, A. Hernas, J. Mater. Process. Technol. 53 (1996) 101.
[9] S.K. Sahay, H.K.D.H. Bhadeshia, R.W.K. Honeycombe, Mater. Sci. Eng. A A157 (1992) 101.
[10] J. Janovec, A. Vyrostkova, M. Svoboda, Metall. Mater. Trans. A 25 (1994) 1543.
[11] J. Hucińska, Mater. Corros. 55 (2004) 292.
[12] J. Mc Call, M. Mueller, Metallographic Specimen Preparation, Plenum Press, 1974.
[13] Metals Handbook, Metallography and Microstructures, vol. 9, ASM, 1985.
[14] V. Voort, Metallography: Principles and Practice, Mc Graw-Hill, 1984.
[15] F. Bell, D.E. Sonon, Improve Metallographic Etching, vol. 9, 1976.
[16] G. Petzow, Metallographic Etching, American Society for Metals ASM, 1978.
[17] M. Louthan, Optical Metallography, Departament of Materials, U Virginia Polytechnics Institute, 1985.

[18] B. Beeston, Electron Doffraction and Optical Diffraction Techniques, North Holland Publishing Co, 1972.

[19] K.H. Pyo, P.J. Kyu, L.Y. Soo, K.J. Soo, 16th International Conference on Structural Mechanics in Reactor Technology Transactions SMiRT, vol. 16, paper 1095, 2001.

[20] ASTM Standards, Annual Book, Metallograpy Nondestructive Testing, vol. 03.03, ASTM, Philadelphia, 1984.

[21] J.C. Russ, Uses of the Electron Microscope in the Materials Science, STP 480, ASTM, Philadelphia, 1970, p. 214.

[22] R.L. Lee, J.F. Kelly, Pract. Metallogr. 21 (1984) 27.

[23] J.W. Harle, The Use of the Scanning Electron Microscope, Pergamon Press, 1972.

[24] H. Mc Gannon, The Making and Treating of Steel, ninth ed., ASTM, United Steel, 1971, p. 1220.

[25] B.E. Peddle, C.A. Pickles, Can. Metall. Quart. 40 (2001) 105.

[26] N. Fujita, H.K.D.H. Bhadeshia, ISIJ Int. 42 (2002) 760.

[27] C. Toh, P. Munroe, D. Young, Oxid. Met. 58 (2002) 1.

[28] D.V. Shtansky, G. Inden, Acta Mater. 45 (1997) 2861.

[29] A.K. Ray, Y. Tiwari, K. Roy, S. Chaudhuri, S. Bose, R. Ghosh, J. Whittenberger, Mater. Sci. Eng. A 454–455 (2007) 679.

[30] G. Landrum, W. Glassey, Yet Another Extended HuckelMolecular Orbital Package (YAeHMOP), Cornell University, Ithaca, NY, 2004.

[31] D. Tzeli, A. Mavridis, J. Chem. Phys. 116 (2001) 4901.

[32] Amsterdam Density Functional Package Release, Vrije Universiteit, Amsterdam, 2001.

[33] R. Wu, A. Freeman, G. Olson, Phys. Rev. B 53 (1996) 7504.

[34] I. Shein, N. Medvedeva, A. Ivanovskii, Physica B 371 (2006) 126.

[35] R. Fournier, J. Andzeim, A. Goursot, N. Russo, D. Salahub, J. Chem. Phys. 93 (1990) 2919.

[36] W.C. Chiou, E.A. Carter, Surf. Sci. 530 (2003) 1.

[37] R. Wyckoff, Crystal Structures, second ed., Interscience, New York, 1963.

[38] A. Juan, R. Hoffmann, Surf. Sci. 421 (1999) 1.

[39] R. Hoffmann, W.N. Lipscom, J. Chem. Phys. 36 (1962) 2179.

[40] R. Hoffmann, J. Chem. Phys. 39 (1963) 1397.

[41] M.H. Whangbo, J. Am. Chem. Soc. 100 (1978) 6093.

[42] A.B. Anderson, J. Chem. Phys. 62 (1975) 1187.

[43] D. Becke, Phys. Rev. A 38 (1988) 3098.

[44] C. Lee, W. Yang, R.G. Parr, Phys. Rev. B 37 (1988) 785.

[45] B.V. Reddy, S.C. Deevi, A.C. Lilly, P. Jena, J. Phys.: Condens. Matter 13 (2001) 8363.

[46] M.R. Press, T. Liu, S.N. Khanna, P. Jena, Phys. Rev. B 40 (1989) 399.